



HAL
open science

Statistical Analysis of the Radial Evolution of the Solar Winds between 0.1 and 1 au and Their Semiempirical Isopoly Fluid Modeling

Jean-Baptiste Dakeyo, Milan Maksimovic, Pascal Démoulin, Jasper Halekas, Michael Stevens

► **To cite this version:**

Jean-Baptiste Dakeyo, Milan Maksimovic, Pascal Démoulin, Jasper Halekas, Michael Stevens. Statistical Analysis of the Radial Evolution of the Solar Winds between 0.1 and 1 au and Their Semiempirical Isopoly Fluid Modeling. *The Astrophysical Journal*, 2022, 940 (2), pp.130. 10.3847/1538-4357/ac9b14 . obspm-03905443

HAL Id: obspm-03905443

<https://hal-obspm.ccsd.cnrs.fr/obspm-03905443>

Submitted on 18 Dec 2022

HAL is a multi-disciplinary open access archive for the deposit and dissemination of scientific research documents, whether they are published or not. The documents may come from teaching and research institutions in France or abroad, or from public or private research centers.

L'archive ouverte pluridisciplinaire **HAL**, est destinée au dépôt et à la diffusion de documents scientifiques de niveau recherche, publiés ou non, émanant des établissements d'enseignement et de recherche français ou étrangers, des laboratoires publics ou privés.

Statistical Analysis of the Radial Evolution of the Solar Winds between 0.1 and 1 au, and their Semi-empirical Iso-poly Fluid Modeling

2 JEAN-BAPTISTE DAKEYO ^{1,2} MILAN MAKSIMOVIC ¹ PASCAL DÉMOULIN ^{1,3} JASPER HALEKAS ⁴ AND
3 MICHAEL L. STEVENS ⁵

4 ¹LESIA, Observatoire de Paris, Université PSL, CNRS, Sorbonne Université, Université de Paris, 5 place Jules Janssen, 92195 Meudon,
5 France

6 ²IRAP, Observatoire Midi-Pyrénées, Université Toulouse III - Paul Sabatier, CNRS, 9 Avenue du Colonel Roche, 31400 Toulouse, France

7 ³Laboratoire Cogitamus, 75005 Paris, France

8 ⁴Department of Physics and Astronomy, University of Iowa, Iowa City, IA 52242, USA

9 ⁵Smithsonian Astrophysical Observatory, Cambridge, MA, USA

10 ABSTRACT

11 Statistical classification of the Helios solar wind observations into several populations sorted by bulk
12 speed has revealed an outward acceleration of the wind. The faster the wind is, the smaller is this
13 acceleration in the 0.3 – 1 au radial range (Maksimovic et al. 2020). In this article we show that recent
14 measurements from the Parker Solar Probe (PSP) are compatible with an extension closer to the Sun of
15 the latter Helios classification. For instance the well established bulk speed/proton temperature (u, T_p)
16 correlation and bulk speed/electron temperature (u, T_e) anti-correlation, together with the acceleration
17 of the slowest winds, are verified in PSP data. We also model the combined PSP & Helios data, using
18 empirical Parker-like models for which the solar wind undergoes an "iso-poly" expansion: isothermal in
19 the corona, then polytropic at distances larger than the sonic point radius. The polytropic indices are
20 derived from the observed temperature and density gradients. Our modelling reveals that the electron
21 thermal pressure has a major contribution in the acceleration process of slow and intermediate winds
22 (in the range of 300-500 km/s at 1 au), over a broad range of distances and that the global (electron
23 and proton) thermal energy, alone, is able to explain the acceleration profiles. Moreover, we show that
24 the very slow solar wind requires in addition to the observed pressure gradients, another source of
25 acceleration.

26 *Keywords:* space physics — solar wind — acceleration process — thermal pressure — data analysis

27 1. INTRODUCTION

28 In the hydrodynamic description, the solar wind
29 comes from the thermal expansion of the million Kelvin
30 solar corona which cannot remain in hydrostatic equi-
31 librium around the Sun. Indeed, as firstly establish by
32 Parker (1958), the solar wind is the result of the conver-
33 sion of the coronal thermal energy into directed kinetic
34 energy. This implies the generation of a flow which be-
35 comes supersonic at a distance (r_c) of a few solar radii
36 from our star.

37 Many authors have studied the radial evolution of
38 the thermodynamic properties of the solar wind, using
39 the large coverage of heliocentric distances allowed by

40 the Helios missions (Schwartz & Marsch 1983; Hellinger
41 et al. 2011, 2013; Štverák et al. 2015; Maksimovic et al.
42 2020). In an attempt to disentangle the temporal from
43 the radial variations of the solar wind, Schwartz &
44 Marsch (1983) have applied the technique of radial line-
45 ups, where they have studied a single piece of solar wind
46 as seen at two different heliocentric distances. They have
47 observed a radial compression of the flux tube, that can
48 be an illustration of wind interactions (co-rotating inter-
49 action regions). In order to study the heating, Hellinger
50 et al. (2011) and Hellinger et al. (2013) compare, respec-
51 tively for the slow and fast winds, the heating needed to
52 get the observed proton temperature gradients (parallel
53 and perpendicular), to the heating rates deduced from
54 the radial wind speed. Both studies strongly suggest an
55 efficient transfer of thermal energy from the parallel to
56 the perpendicular direction to be in accordance with the

57 proton temperature gradients. Other authors as Štverák
58 et al. (2015) have made similar analysis on the electrons,
59 and have shown that the observed empirical radial pro-
60 files do not require any external heat source (heat flux
61 and its divergence) to explain the observed electron tem-
62 perature gradients, for both slow and fast representative
63 solar wind streams.

64 More recently, Maksimovic et al. (2020), inspired by
65 the work of Totten et al. (1995), have classified the dif-
66 ferent winds observed by Helios according to their ve-
67 locity, imposing the same order between velocity pop-
68 ulations at all distances. They have shown that the
69 correlation bulk speed/proton temperature (u , T_p) and
70 the anti-correlation bulk speed/electron temperature (u ,
71 T_e), first found around 0.7 au, extends until 0.3 au (the
72 closest approach distance of Helios missions). In the
73 present work we use the same wind classification tech-
74 nique as Maksimovic et al. (2020) and extend it to PSP
75 data closer to the Sun.

76 After Parker’s seminal work, a great number of au-
77 thors have proposed semi-empirical fluid models of the
78 solar wind, imposing remote sensing observations as
79 boundary conditions in the corona (Esser et al. 1997;
80 Cranmer et al. 1999; Sanchez-Diaz et al. 2016). These
81 authors have often used more or less ad’hoc sources of
82 energy, in addition to the thermal one, allowing them to
83 reproduce observations at 1 au. Another approach is to
84 develop solar wind models including the observed poly-
85 tropic indices as deduced from the temperature and den-
86 sity gradients. For instance Cranmer et al. (2009) em-
87 pirically constrain fast wind modeling by the observed
88 proton and electron temperature radial dependencies,
89 using a turbulent hydrodynamic model.

90 Coronal observations in coronal holes and streamers
91 can provide observational constraints to solar wind mod-
92 els. For a medium solar wind ($\sim 350 - 500$ km/s at 1 au
93) the proton coronal temperature is found in the range
94 1 - 3 MK, and the electron coronal temperature within
95 0.5 - 1 MK (Cranmer et al. 1999; Cranmer 2002; David
96 et al. 1998). However concerning the fast wind, which
97 has been well established to come from coronal holes,
98 the hydrogen kinetic temperatures are possibly as large
99 as 4 - 6 MK (Kohl et al. 1996; Cranmer 2002). Then,
100 with enough collision coupling in the low atmosphere,
101 the proton temperature is also expected to be in this
102 range. Regarding the temperature of electrons in coro-
103 nal holes, it is well established to be lower than in the
104 streamer belt.

105 In the present approach we also develop a semi-
106 empirical model. In contrast with previous works which
107 start from the observed coronal constraints, we rather
108 base our model on the interplanetary observations, then

109 we derive the expected coronal values. To do this, we
110 use a Parker polytropic model far from the Sun which
111 includes proton and electron pressure contributions sep-
112 arately. In order to avoid excessive coronal tempera-
113 ture, we include an isothermal solution closer to the Sun.
114 This defines our ”iso-poly” fluid model. The polytropic
115 indices and temperatures for both the protons and elec-
116 trons in the interplanetary medium are derived from ob-
117 servations of the two missions Helios (Porsche 1981) and
118 Parker Solar Probe (Fox et al. 2016).

119 In Section 2, we first describe the data sets we use, and
120 how we define the different wind populations. Then, we
121 analyze how the new PSP data compare to the Helios
122 ones within the overlapping range of solar distances. Af-
123 ter that, we classify the PSP data the same way as for
124 Helios, and we check whether the radial trends observed
125 for the bulk speed and the temperature gradients in the
126 0.3 - 1 au range, could be extended closer to the Sun.
127 In Section 3, we describe our iso-poly fluid model, and
128 the way its free parameters are constrained by the ob-
129 servations. Finally, we summarize our results in Section
130 4. More information and details on the iso-poly model
131 are provided in the appendixes B - C.

132 2. WIND POPULATIONS FROM HELIOS AND PSP 133 OBSERVATIONS

134 2.1. Revisited Helios Measurements

135 In this section, we revisit the analysis made by Mak-
136 simovic et al. (2020) by removing from the datasets the
137 periods corresponding to interplanetary coronal mass
138 ejections (ICMEs). This was not done in the original
139 study. We use two of the Helios data sets used by Mak-
140 simovic et al. (2020). They are derived from the ion
141 and electron electrostatic analyzers on board the Helios
142 1 and 2 spacecraft (Schwenn et al. 1975). The first data
143 set contains $\sim 1\,877\,000$ measurements of proton den-
144 sity n_p , temperature T_p and bulk speed u . The second
145 one, made by Štverák et al. (2009), contains $\sim 66\,000$
146 measurements of electron density n_e and temperature
147 T_e . One can find more details about the used Helios
148 data set in Maksimovic et al. (2020). We also choose to
149 only keep the Helios measurements during the minimal
150 solar activity (from 1974 until 1977), in order to be able
151 to compare the same solar activity level with the PSP
152 observations.

153 We remove ICMEs from our Helios data set using the
154 criteria of Elliott et al. (2012). We discard the measure-
155 ments for which at least one of the following criteria on
156 the β of the plasma, the proton temperature T_p , and the
157 ratio of the alpha to proton density n_α/n_p , is satisfied:
158 (i) $\beta < 0.1$, (ii) $n_\alpha/n_p > 0.08$, (iii) $T_p/T_{ex} < 0.5$, where
159 T_{ex} is a temperature predicted by a scaling law estab-

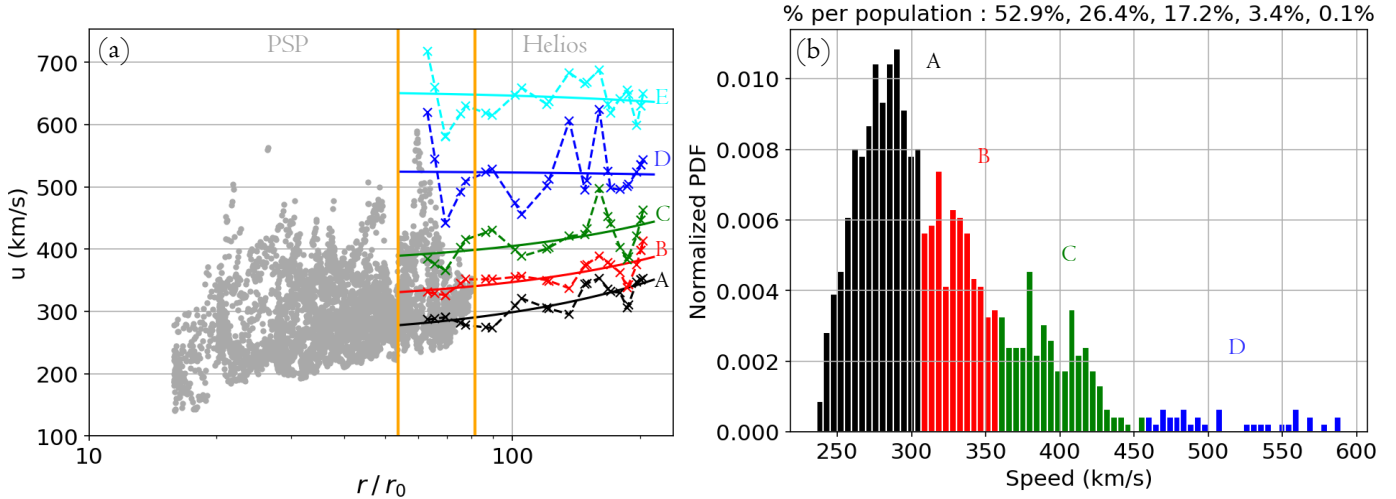


Figure 1. (a) Median proton bulk speed, $u(r)$, in colored dashed lines for 5 populations from Helios measurements of bulk speed between 0.3 and 1 au (where r_0 the solar radius). The data are first regrouped within radial bins, then the wind populations are defined with quantiles (Maksimovic et al. 2020). The linear fits of the Helios speed populations, $u(r)$, are shown with colored solid lines. The PSP measurements from SPAN-Ai and SPC instruments are plotted with grey points. The two orange vertical lines delimit the overlap interval of SPC and Helios data (0.28 - 0.38 au). **The mean errors on the estimation of the median values for the different quantities are :** $\delta u_{|\text{Hel1}} = 0.1\%$, $\delta T_{p|\text{Hel1}} = 0.6\%$, $\delta T_{e|\text{Hel1}} = 1.3\%$, $\delta n_{e|\text{Hel1}} = 1.5\%$, **with the error defined as:** σ/\sqrt{N} with σ the standard deviation and N the number of data points per populations on each bin. (b) Probability distribution function of bulk speed of SPC on the overlap interval PSP - Helios. These data are classified using the Helios quantiles.

lished by Lopez & Freeman (1986) and rescaled with solar distance. In addition to these criteria, we remove for every detected ICME of at least 6 hours long, the 24 hours before and 15 hours after it. Finally, we assume that winds measurement faster than 800 km/s could be possible ICMEs, so that we also remove them. Our final Helios data set contains $\sim 686\ 000$ proton measurements and $\sim 65\ 000$ electron measurements.

With such data, a possible way to study the solar wind evolution with distance is to classify it into wind populations, determined by a statistical classification of protons speed measurements at different radial distances, as it was done by Maksimovic et al. (2020). Wind speed observations are first split in radial bins, then for each bin, the bulk velocity distribution is divided with quantiles to classify winds depending on their speed. The median of each speed population is kept. This defines a set of median velocities versus distance as shown in dashed colored lines in Figure 1a. This classification method assumes that the wind population order does not change with solar distance. We have made the same choice as Maksimovic et al. (2020) to set 5 wind populations, named from **A** for the slowest one, to **E** for the fastest one. This choice of the number of populations is somewhat arbitrary, but we have verified that the results of our study do not depend on this number. The Helios populations have wind speeds ranging between 250 km/s

and 700 km/s (Figure 1a). The slower the wind is, the more progressive is its acceleration with radial distance, until the **E** wind for which the speed is approximately constant in the studied range. Note that our slow wind population is very similar to the "very slow solar wind" studied by Sanchez-Diaz et al. (2016).

2.2. PSP Measurements

There are on board PSP three instruments part of the SWEAP suite (Kasper et al. 2016) which measure solar wind bulk speed, temperature and density: the Solar Probe Cup (SPC), the Solar Probe ANalyser Ion (SPAN-Ai) both for protons, and the Solar Probe ANalyser Electron (SPAN-E) for electrons. The purpose of the present subsection is to establish a single PSP data set, associating for each of the individual times of measurements, one proton and one electron measurement over the largest possible range of solar distances.

Since the SPC instrument is based on the classical design of a Faraday Cup, which measures the protons along the radial field of view, its data have some drawbacks close to the Sun. Because the probe has a very large tangential speed close to the Sun, fewer solar wind protons can enter the radial field of the instrument, causing the measurements to be biased. The slower the wind speed is, the more this effect is important, especially around perihelion since the tangential probe speed has the same

order as the radial slow wind speed. Looking to the encounters 4 to 9 SPC data on the relevant servers, we have observed empty regions of measurements closer to the Sun, partly due to this effect. We have thus decided to remove SPC data under 0.2 au ($\sim 43 R_{\odot}$) to avoid these gaps.

The SPAN-Ai (SPI) instrument is performing more efficiently closer to the Sun than farther away, because of a better configuration of the field of view due to the tangential motion of the spacecraft (Kasper et al. 2016). The SPI Data Release Notes from NASA documentation indicates that the instrument mainly provides data below 0.25 au ($\sim 53 R_{\odot}$). Therefore, we need SPC data at larger solar distances to have an overlap of distances with Helios data.

With the aim of making the radial coverage between SPI and SPC data instruments, we have compared the speed and the temperature (L3 moments) given by the two instruments. The speeds are comparable, while the temperatures are not as close. Indeed, comparing only the radial temperature moment for the two instruments during periods where the solar wind proton peak falls in the joint field of view for both SPAN-Ai and SPC, we note that these measurements typically differ by $T_{r|SPI} \sim 2 T_{r|SPC}$. Secular trends in time and space are consistent between the two instruments, suggesting that the difference between the two must be some systematic error. An inspection of proton core peak widths over such periods shows consistency between the two instruments, however the SPAN-Ai instrument consistently resolves the extended tails of the proton distribution function out to more extreme speeds and lower fluxes (**Davin Larson, Michael Stevens, private communication**). We therefore hypothesize that the systematic error is a manifestation of the energy partition between the Maxwellian or nearly-Maxwellian part of the proton core and the remaining non-thermal part of the solar wind proton distribution function, where the SPC measurement is dominated by the former while SPAN-Ai moment includes the latter.

To generate a consistent temperature record that combines both SPAN-Ai and SPC in order to cover the largest range of solar distances, we have applied an empirical factor of 2 to the SPC temperatures that is designed to incorporate the non-thermal tail component. We have furthermore empirically adjusted the SPC measurements to account for proton anisotropy, as the SPC measurement is purely radial. For that correction, we use the ratio $T_{r|SPI}/T_{tot|SPI}$ which evolves approximately linearly with solar distance, providing a linear anisotropy ratio with radial distance (Appendix A).

Doing so an equivalent total proton temperature is established from $T_{r|SPC}$ assuming the same anisotropy ratio over the distances covered by SPC. In this way we set an equivalent 3D total proton temperature on larger solar distances.

The SPAN-E (SPE) instrument measures the full electron VDFs in the solar wind. The electron data we use are obtained with the fitting techniques described in Halekas et al. (2020). The total temperature and total density have been obtained by integration of the VDFs after removing the photo-electron and secondary electron contribution.

Considering all the experimental limitations, we have used SPI data below 0.25 au, SPE data below 0.37 au and SPC data from 0.2 to 0.37 au. For every measurement time where we have both SPI and SPC data, we have kept the mean value. For density measurements, we have made the choice to show only n_e data from SPE (Halekas et al. 2020). Indeed, without measurements of the alpha particles density on the entire studied radial range, it is more relevant to use n_e to estimate the total density of the plasma.

The PSP observations cover 5 encounters, from E4 to E9, combining in total 2237 hours of measurement for u , T_p , T_e and n_e . The quantity of data to treat are large because of the high sample rates, especially for SPC. Since in any case we bin the data by distance, we have computed average values of the above parameters over 30 minutes.

The bulk speed averages are shown as grey dots in Figure 1a. It appears that PSP has mainly measured slow and intermediate winds (from 150 km/s to ~ 500 km/s) since its launch. Indeed, since the observational interval corresponds to a period of minimum of solar activity, the fast solar wind in the ecliptic plane is rarely measured.

2.3. How well PSP Data Extend Helios ones?

With the purpose of defining the wind populations closer to the Sun, we have determined to what extent the Helios populations are represented in the PSP data coverage. To do this, we have defined an overlap interval between Helios and PSP, represented by the two orange vertical lines in Figure 1a. This overlap ranges from 0.28 to 0.38 au.

In the overlap interval, we have classified the PSP data points (grey points on Figure 1a) attributing them one of the populations defined from Helios measurements. For this purpose we compare the bulk speeds between the two probes. We assign each PSP measurement to the Helios population to which it is the closest. To have smoother representation of the Helios median pop-

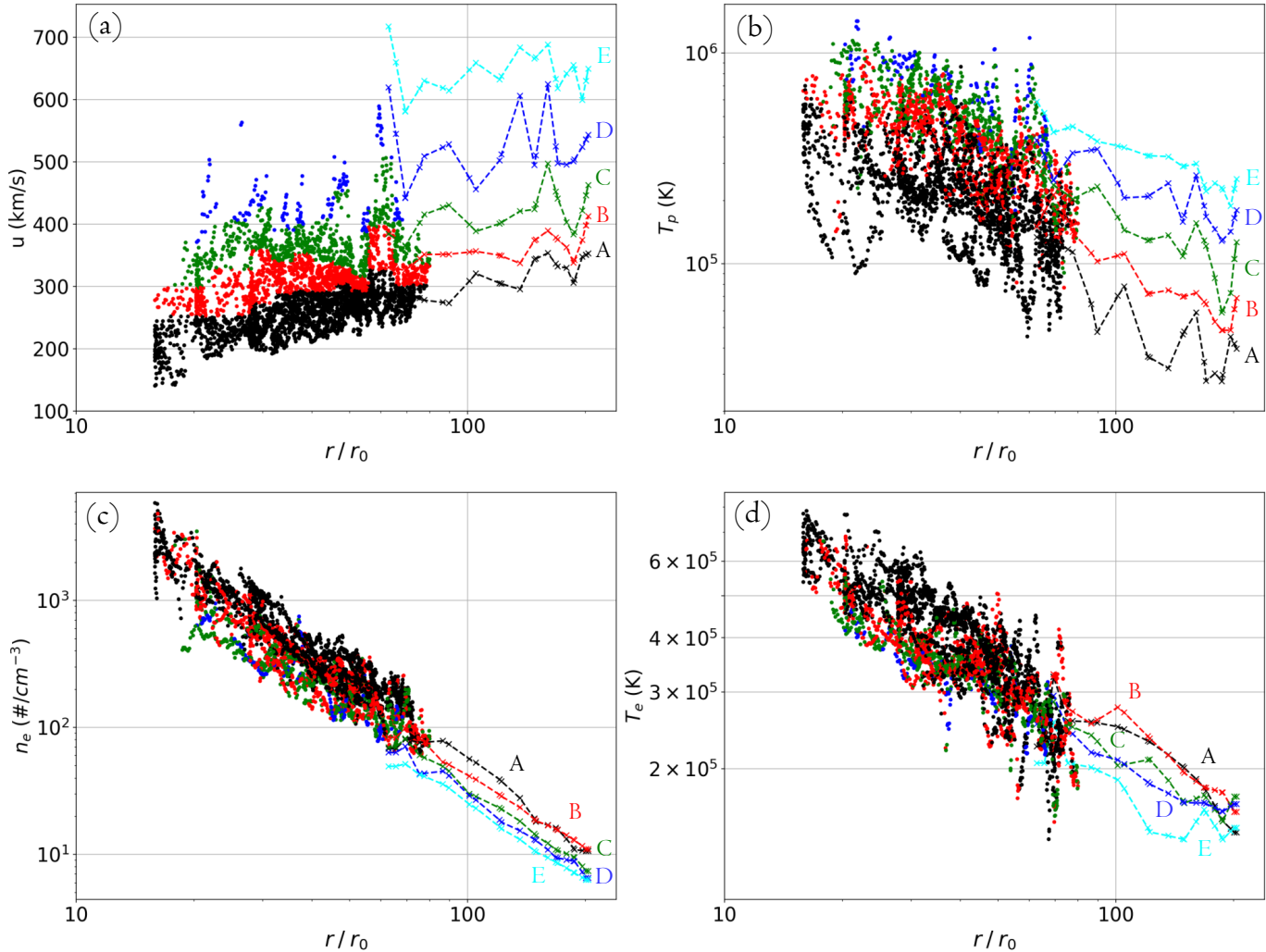


Figure 2. Classification of $u(r)$, $T_p(r)$, $T_e(r)$ and $n_e(r)$ from PSP data set (colored dots). The PSP population percentage is defined in the overlap interval (Figure 1) by assigning each PSP data to the closest Helios population. The median values of the 5 Helios populations are added with colored dashed lines as in Figure 1a.

315 ulations profiles (colored dashed lines on Figure 1a),
 316 we have considered their main tendency using the least
 317 square fitted straight lines (represented in solid lines on
 318 the same panel).

319 The percentage of PSP data corresponding to the He-
 320 lios populations **A** to **E** are represented on Figure 1b
 321 with the same color code as for the previously estab-
 322 lished populations. It appears that the two fastest wind
 323 populations are much less represented than the others
 324 in PSP measurements, with only 3.4 % for the wind **D**
 325 and 0.1 % for the wind **E** within the overlap interval.
 326 Therefore, the wind **E** cannot be studied close to the
 327 Sun.

328 The determined percentages ensure that the PSP mea-
 329 surements are classified in accordance with Helios popu-
 330 lations. Next, we divide PSP radial range in 10 intervals
 331 with the same number of data, then we apply the quan-

332 tile classification with the percentage obtained from the
 333 overlap interval. Instead of quintiles (20%) for each of
 334 the HELIOS populations **A** to **E**, we classify the PSP
 335 data, within a given radial bin, according to the per-
 336 centages defined in Figure 1b (52.9% for the wind **A**,
 337 26.4% for wind **B**, 17.2% for **C** and the remaining 3.5%
 338 for **D**). The PSP data with this classification are shown
 339 on Figure 2.

340 We observe a continuation of the radial trends be-
 341 tween Helios and PSP, for all the displayed parameters
 342 (while only the bulk speed is used in the overlap inter-
 343 val to define the PSP populations). Also some regions
 344 without bulk speed and proton temperature data, par-
 345 ticularly close to the largest and for the smallest solar
 346 distances, are visible on Figure 2. Indeed, PSP has not
 347 spent enough time to measure each population at all so-
 348 lar distances with enough statistics. So for populations

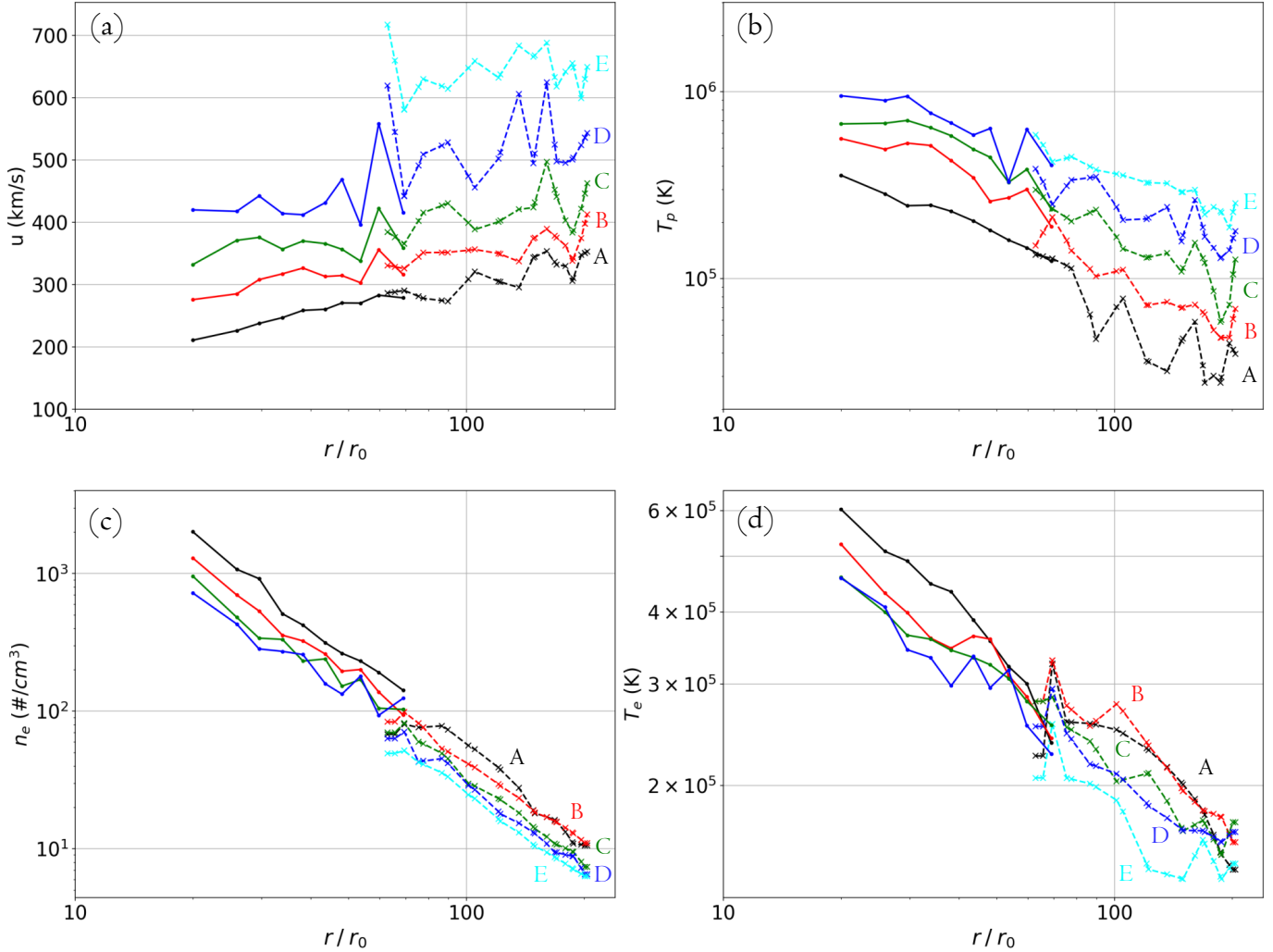


Figure 3. Classification of $u(r)$, $T_p(r)$, $T_e(r)$ and $n_e(r)$ from PSP data set using the percentages defined with Helios data in the overlapping distances of PSP and Helios. The median values of PSP radial bins are represented with points connected with solid lines. The median values of Helios radial bins are represented with crosses connected with dashed lines. **The mean errors on the estimation of the median values for the different quantities are :** $\delta u_{\text{PSP}} = 0.8\%$, $\delta T_p|_{\text{PSP}} = 3.7\%$, $\delta T_e|_{\text{PSP}} = 1.3\%$, $\delta n_e|_{\text{PSP}} = 4.1\%$.

349 which are close to these regions, the analysis might be
350 taken with caution.

351 **Regarding the spreading of the different popula-**
352 **tions on the temperature and density (Figure**
353 **2b, 2c and 2d), the populations overlap each oth-**
354 **ers contrarily to the ones in speed (Figure 2a).**
355 **Indeed, the speed populations are directly sepa-**
356 **rated by the quantiles, while the others quan-**
357 **tities are derived from the associated time of**
358 **measurement after classification. Then, to ob-**
359 **tain a better view of the populations evolution**
360 **for each quantity, we compute for each radial bin the**
361 **median value for all the populations and for all quan-**
362 **tities. These are displayed by dots connected with solid**
363 **lines in Figure 3. The mean errors on the deter-**

364 **mination of the median profiles are quite low**
365 **either for PSP or Helios data :** $(\delta u_{\text{PSP}}, \delta u_{\text{Helios}}) =$
366 $(0.8\%, 0.1\%)$, $(\delta T_p|_{\text{Helios}}, \delta T_p|_{\text{PSP}}) = (3.7\%, 0.6\%)$,
367 $(\delta T_e|_{\text{Helios}}, \delta T_e|_{\text{PSP}}) = (1.3\%, 1.3\%)$, $(\delta n_e|_{\text{Helios}}, \delta n_e|_{\text{PSP}}) =$
368 $(4.1\%, 1.5\%)$. **Moreover, considering all quanti-**
369 **ties, the errors do not exceed 4.1%, which means**
370 **that the computed median values are well de-**
371 **finied. As previously mentioned for Figure 2, the PSP**
372 **populations are globally the continuation of the Helios**
373 **ones. This is true for the amplitude of the bulk speed**
374 **following the definition of the populations in the overlap**
375 **interval. However, the speed trends are also comparable**
376 **between PSP and Helios, while constrained.**

377 Next, proton temperatures from PSP are consistent
378 with a continuation of Helios data (with large fluctua-

tions for the wind **D** in the overlap interval due to data gaps). Electron densities of PSP data extend the Helios power laws closer to the Sun. Finally, electron temperatures have large fluctuations in and around the overlap interval. Still outside this region, PSP data are in accordance with the extensions of the Helios power laws with distances.

The higher variations for the farther radial point of the wind **B**, **C** and **D** for all PSP parameters are probably due to the regions empty of data in Figure 2 as mentioned above. Next, we notice that the proton temperature for the winds **B**, **C** and **D**, seems to stop increasing closer to the Sun. However, considering the lack of good statistical coverage for the radial bins closer to the Sun, no definitive interpretation can be made presently. Indeed, to have a more reliable analysis of the slope in the radial bins closer to the Sun, a longer observational time interval is necessary.

All the observational results shown on the PSP radial range regarding the radial dependencies of the temperature populations and the acceleration of the slow solar wind, are also confirmed by a different radial analysis method of the solar winds evolution of Halekas (2022, in press).

3. COMPARISON BETWEEN OBSERVATIONS AND MODELING RESULTS

3.1. Hydro-dynamic Model Limitations

Isothermal Parker's model solutions are convenient because they can provide both an analytical expression of the sonic point location and the dependence of the terminal bulk speed with coronal temperature. However, this description requires an infinite energy deposit to maintain the isothermal temperature at all distances.

A more physical description implies taking into account that the observed solar wind temperature is decreasing with distance. As discussed in Section 1, solar wind fluid models using observed polytropic indices have already been proposed. However extrapolating temperature back to the corona, the deduced proton coronal temperature is too high compared to spectroscopic observations, especially for fast winds.

Thus, it could be interesting to mix up isothermal and polytropic approaches. An isothermal expansion can produce a supersonic wind relatively close to the Sun. At larger distances, a polytropic expansion only mildly accelerates the wind, while it reproduces the observed decrease of temperature with distance. This iso-poly model takes the best of each approach while putting aside their respective major physical issues (infinite deposit of energy for the isothermal case, and too high coronal temperature for the polytropic one). Note

that Parker (1960) has also proposed a two thermal part model, with an isothermal evolution close to the Sun, then adiabatic farther away. However, this description disagree with in-situ measurements of temperature (magnitude and radial evolution), and with the observed acceleration of slow winds on large distance.

3.2. Iso-poly Solar Wind Model

The equations we develop in this article embed the possibility of two consecutive thermal regime for the solar wind. We set the following hypotheses: (i) We consider a bi-fluid constituted of electrons and protons, with $u_e = u_p = u$, $n_e = n_p = n$, $T_e \neq T_p$ and $\gamma_e \neq \gamma_p$, with no electric current. (ii) We take into account the thermal pressure gradients and gravity as a source of external force. (iii) The problem is studied in the hypothesis of spherical symmetry: $\partial/\partial\theta = \partial/\partial\phi = 0$. (iv) A stationary flow is modeled. (v) The non-thermal effects of the magnetic field on the plasma are neglected.

The transition between the two thermal regimes, isothermal and polytropic, is set at the radius $r_{\text{iso|p}}$ and $r_{\text{iso|e}}$ respectively for protons and electrons. These distances are expected to be different for these two species because different heating/cooling processes are present and because a low collisional coupling occurs between the two species in the considered radial range (Cranmer 2002). Next, in order to simplify the expressions below, we only specify the species with $s = \{p, e\}$, and we write the sum over these species when needed.

The model incorporates in-situ observational constraints for both electrons and protons with a polytropic law:

$$T_s(r) = T_{s0} \left(\frac{n(r)}{n_{\text{iso|s}}} \right)^{\gamma_s - 1} = T_{s0} \tilde{n}_s^{\gamma_s - 1}. \quad (1)$$

where γ_s is constrained by in-situ observations to be uniform in the PSP and Helios radial range, while dependant of the wind population and specie. We introduce the density at $r = r_{\text{iso|s}}$, $n_{\text{iso|s}}$, within Equation (1) in order to have a formula valid both for $r < r_{\text{iso|s}}$ ($\gamma_s = 1$, isothermal, $T_s(r) = T_{s0}$) and for $r > r_{\text{iso|s}}$ ($\gamma_s > 1$, for constant value), and $T_s(r)$ is continuous at $r = r_{\text{iso|s}}$. The notation $\tilde{n}_s = n(r)/n_{\text{iso|s}}$ is introduced to simplify the writing of the following equations.

The conservation of momentum is written as:

$$n m_p u \frac{du}{dr} = - \sum_{s=\{p,e\}} \frac{dP_s}{dr} - n m_p \frac{GM}{r^2}. \quad (2)$$

For a given thermal profile, e.g., Equation (1), the pressures P_s are proportional to the plasma density. Indeed, all terms in Equation (2) are linear in n so multiplying the density by any factor (independent of r) has no

Wind type	A	B	C	D	E
γ_p	1.57	1.59	1.52	1.44	1.35
γ_e	1.29	1.24	1.23	1.23	1.21
$r_{\text{iso p}} (R_\odot)$	16.1	16.4	13.6	9.2	2.9
$r_{\text{iso e}} (R_\odot)$	15.0	9.8	10.3	8.0	3.1
T_{p0} (MK)	0.65	1.10	1.63	2.51	5.61
T_{e0} (MK)	0.79	0.81	0.71	0.75	0.88
u_0 (km/s)	0.001	0.07	0.6	7	104
$u_{1\text{au}}$ (km/s)	292	354	406	488	634

Table 1. Parameters of the iso-poly model (four top lines). Resulting the coronal temperatures T_{p0} , T_{e0} , and the coronal and at 1 au velocities u_0 and $u_{1\text{au}}$ (four bottom lines). The parameters are defined by least square fitting the model to temperatures and velocities derived from PSP and Helios measurements for the wind populations from **A** to **D**, and only from Helios measurements for the population **E** (see Figure 4).

effect on u . The pressures P_s are written similarly to temperatures in Equation (1):

$$P_s = P_{s,\text{iso|s}} \left(\frac{n}{n_{\text{iso|s}}} \right)^{\gamma_s} = P_{s,\text{iso|s}} \tilde{n}_s^{\gamma_s}. \quad (3)$$

Then, Equation (2) is rewritten as:

$$n m_p u \frac{du}{dr} = - \sum_{s=\{p,e\}} \left(P_{s,\text{iso|s}} \frac{d\tilde{n}_s^{\gamma_s}}{dr} \right) - n m_p \frac{GM}{r^2}. \quad (4)$$

Next, the computation of $n(r)$ is deduced only from $u(r)$ using the mass flux conservation:

$$n(r) = \frac{C_n}{u r^2}, \quad (5)$$

where C_n is a constant to be determined for each population with a fit to the in-situ data. This Equation allows to eliminate n in Equation (4). After several steps of calculation, Equation (4) is transformed to outline the critical or sonic point located at $r = r_c$ (see Equation (B8) in Appendix B). This allows to define the transonic solution for which the derivative du/dr is non-zero for all r values. Finally, $u(r)$ is numerically computed (see Appendix B), then $n(r)$ and $T_s(r)$ are computed with Equations (5) and (1).

3.3. Iso-poly Modeling of the Wind Populations

We describe below how the iso-poly model parameters are constrained with in-situ data. Our iso-poly model has a priori six free parameters: γ_p , γ_e , T_p , T_e , $r_{\text{iso|p}}$ and $r_{\text{iso|e}}$.

The polytropic indices can be determined from temperature and density gradient observations. Indeed,

considering power law evolution of the form $T_s(r) \propto r^\alpha$, and $n(r) \propto r^\beta$, the polytropic relation between density and temperature implies $\gamma = (\beta + \alpha)/\beta$. From the mass flux conservation, density for proton and electron are weakly dependent of $u(r)$ profile once the main acceleration region is overcome, thus $\beta \approx -2$. We operate a least square fit on $T_p(r)$ and $T_e(r)$. The radial dependence of T_p and T_e is not the same for all the wind populations, so we fit the α_p and α_e using a linear regression in a log/log space independently for each wind populations. The fitted values of γ_p and γ_e are summarized in Table 1.

The fitted power-law of $T_s(r)$ for each speed population implies that when $r_{\text{iso|s}}$ is defined, T_{s0} is also defined in order to have a continuous temperature. Then, the only two parameters which need to be defined are $r_{\text{iso|p}}$ and $r_{\text{iso|e}}$. This is realized by performing a χ^2 minimization between the model and observed velocities (details in Appendix C). The radial range for the χ^2 minimization is set to $r < 0.5$ au ($\sim 105 R_\odot$) for all the populations. This minimization is less constrained for faster solar winds, especially the wind **E** by the lack of data closer to the Sun.

The iso-poly curves associated to the parameters in Table 1 are plotted in Figure 4 with solid lines. As expected the modeling of proton and electron temperatures is globally in accordance with measurements for all the populations. Locally the proton temperature of the modeled profiles **B**, **C** and **D** are overestimated compared to measurements for the closest radial bins to the Sun. However, considering the empty data regions previously discussed in Figure 2a, measurement profiles for these radial bins are expected to be raised closer to the model curves with larger statistics.

The derived coronal proton temperature for all the populations, except **E**, are in the range of observed coronal temperatures in the solar source regions (1 - 3 MK, Cranmer et al. 1999). Similarly, the derived coronal electron temperatures are also in agreement with the observed range of 0.5 -1 MK (David et al. 1998; Cranmer 2002).

All the iso-poly speed profiles globally fit well to the PSP and Helios measurements (Figure 4a). Still, the iso-poly velocity of population **D** is a bit underestimated on the Helios radial range. This could be explained by the fact that few fast winds have been observed by PSP, especially close to the Sun (Figure 2a). Then, this decreases the iso-poly velocity since the least square fit is limited to $r < 105 R_\odot$. Such a difference between observed and iso-poly speeds is not present for the lower speed winds **C** and **B** where the number of data points is much larger. However, the model curve for the slow-

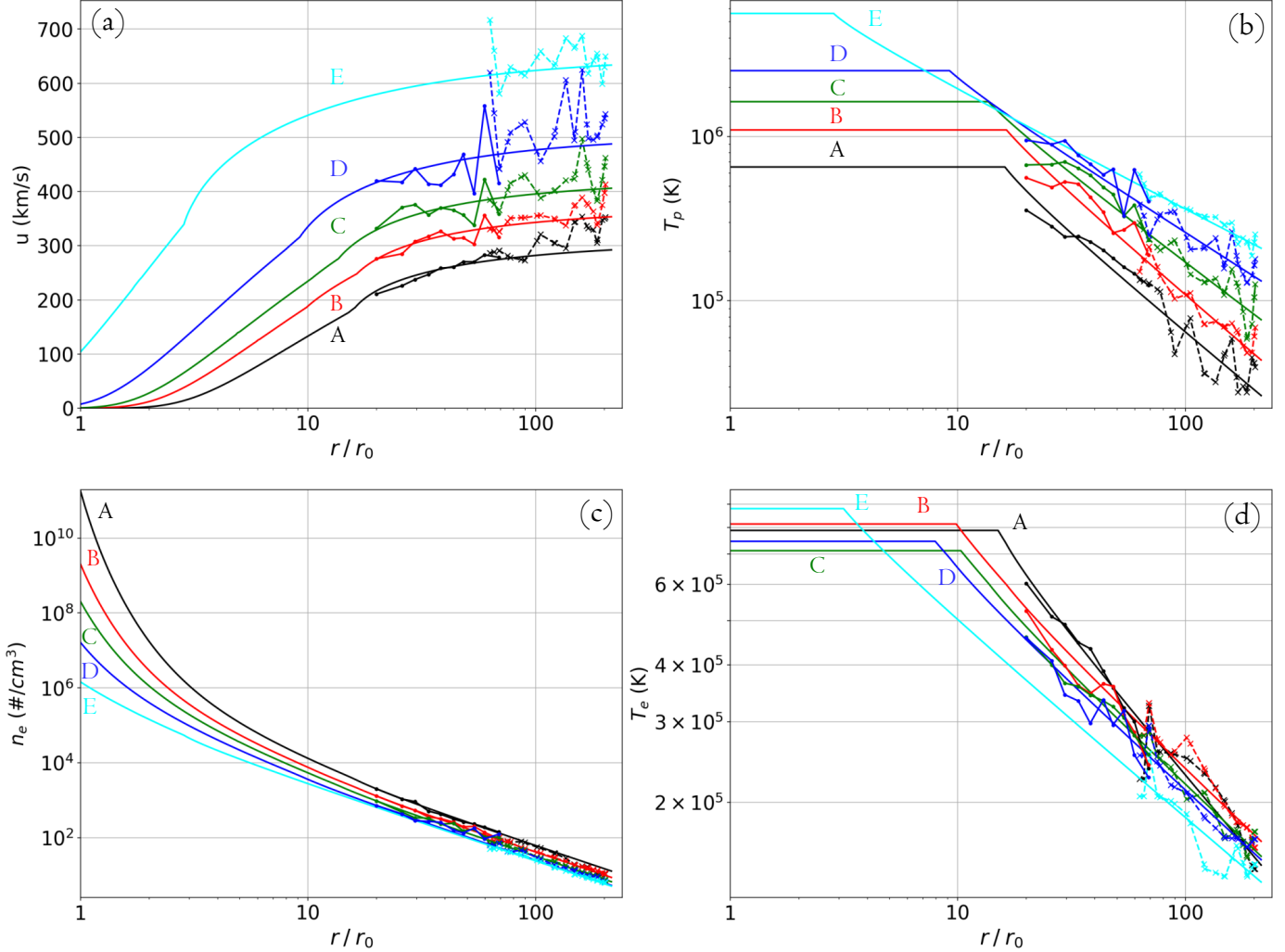


Figure 4. Median values of $u(r)$, $T_p(r)$, $T_e(r)$ and $n_e(r)$ for PSP data (continuous lines linking colored dots) and for Helios data (dashed lines linking colored dots). The iso-poly model curves associated to each family is added with colored continuous lines. They are obtained by least square fitting the radial data profiles.

est wind **A** is lower than its corresponding measurement curve when going farther from the Sun (Figure 4a). This indicates that the observed proton and electron pressures are not efficient enough to accelerate the solar wind as observed. Therefore, the very slow solar wind has another source of acceleration which does not heat the plasma.

The iso-poly model of the fastest wind **E** incorporates only Helios data. The model fits well to all the observed variables (Figure 4); nevertheless, the modeled proton coronal temperature of 5.6 MK is much higher than the 1 - 3 MK observed in the corona. Notice that it is still in the order of the 4 - 6 MK hydrogen temperature observed by Kohl et al. (1996) in coronal holes (possible of the same order as the protons). Concerning the bulk speed close to the Sun, its amplitude is much higher

than for other winds, reaching more than 100 km/s at $1 R_\odot$. This is high for an initial solar wind bulk speed compared to its value at 1 au, however this is not in contradiction with the speed observations made by Sheeley et al. (1997) close to the Sun. Indeed, they have observed at $2 R_\odot$ that wind bulk speed can reach 200 ~ 250 km/s. It concerns mainly slow winds (< 400 km/s at 1 au) but the order of magnitude indicates the possibility of large coronal bulk speeds. This means that the acceleration provided by the observed proton and electron pressure gradients could be not efficient enough to accelerate the fastest wind (in the hypothesis of coronal temperatures in order of 1 - 3 MK). Consequently, the fast wind implies close to the Sun, below 0.3 au ($65 R_\odot$), a temperature higher than the typically observed one in

567 the low corona, and/or another source of energy which
 568 accelerates the plasma and does not heat it.

569 The median plasma densities are well ordered within
 570 PSP distance range. The density is anti-correlated
 571 with the wind speed as observed by Helios and Ulysses
 572 (Marsch et al. 1989; Gloeckler et al. 2003). At lower
 573 solar distances, the densities no longer follow a power
 574 law because of the acceleration of $u(r)$ (Equation (5)).
 575 The wind densities are predicted by the iso-poly model
 576 to spread over a much larger range, up to 5 decades,
 577 when getting closer to the Sun. Next, we compare these
 578 densities to the ones derived during a solar cycle minima
 579 (1996) from LASCO coronagraph. Even if the studied
 580 in-situ data are taken close the ecliptic, we compare the
 581 fast wind density to the one observed around the solar
 582 poles, which are known to be the source of mostly fast
 583 solar wind. The densities derived from the iso-poly mod-
 584 els are compatible with the measurements made above 2
 585 R_{\odot} (Quémerais & Lamy 2002, and also earlier ones, as
 586 summarized therein). The densities derived around the
 587 equatorial plane are expected to be more characteristic
 588 of the slow wind, and indeed the density of population
 589 **B** is close the densities derived from coronagraphic ob-
 590 servations.

591 For the wind populations **A** to **C**, the coronal bulk
 592 speed is very low below $2 R_{\odot}$ (Figure 4a). This implies
 593 large densities (larger than typical coronal densities of
 594 about 10^8 cm^{-3}). However, the iso-poly model is not in-
 595 corporating several key physical processes of the corona,
 596 like thermal conduction and radiative losses, so the re-
 597 gion close to the Sun is out of the range modeled by
 598 the iso-poly model. However, in the range $2 < r < 25$
 599 R_{\odot} the results of Sheeley et al. (1997), obtained with
 600 LASCO coronagraph, are broadly compatible with the
 601 velocity profiles of wind populations **A** to **D**.

602 The positive correlation bulk speed/proton temper-
 603 ature (u, T_p) was originally derived at 1 au (Lopez &
 604 Freeman 1986). The results of the iso-poly model fit-
 605 ted to the in-situ data show that this correlation is kept
 606 down to the solar corona (Figure 4a,b). The results
 607 of the iso-poly model confirm and extend the results of
 608 Démoulin (2009) on the physical origin of the correlation
 609 (u, T_p). This is the result of a dominant wind accel-
 610 eration by the proton pressure close to the Sun (within
 611 $r < 20 R_{\odot}$), with a contribution of electron pressure for
 612 slower winds.

613 In contrast, while a clear anti-correlation between
 614 the electron temperature and the bulk speed is present
 615 above $20 R_{\odot}$, it vanishes closer to the Sun in the iso-poly
 616 modeling (Figure 4d). Indeed, there is no clear trend,
 617 and the coronal temperature, T_{e0} , is similar for all wind
 618 populations (between 0.7 - 1 MK). Thus, in the iso-poly

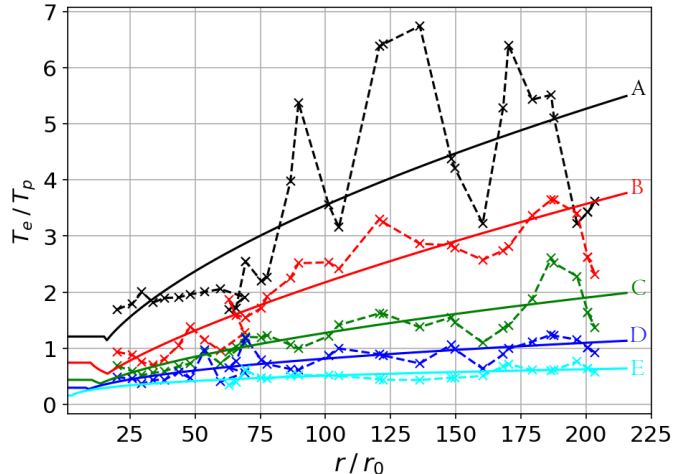


Figure 5. Ratio T_e/T_p for PSP and Helios measurements for all wind populations (dashed lines) as defined in Figure 1. The iso-poly numerical solutions, least square fitted to the data (see Figure 4), are shown with solid curves.

619 description, the different wind populations come from
 620 solar regions with similar electron temperatures.

621 The ratio $T_e/T_p \sim P_e/P_p$ provides evidence of the
 622 species roles in the solar wind dynamics. Far from the
 623 Sun, $r \geq 50 R_{\odot}$, the winds **A**, **B** and **C** are electron
 624 driven, the wind **E** is proton driven, and the wind **D**
 625 has both contributions for $r \geq 100 R_{\odot}$ (Figure 5). In
 626 the main acceleration region for $r < 20 R_{\odot}$, the iso-
 627 poly results indicate that the winds are either proton
 628 and electron driven (**A** and **B**), or proton driven (**C**, **D**
 629 and **E**).

630 The observed electron polytropic indexes, γ_e , are lower
 631 than the proton ones, γ_p , as shown by Maksimovic et al.
 632 (2020) on Helios data, and in Table 1 coupling Helios
 633 and PSP data. Then, T_e radially decreases slower than
 634 T_p , and they have the possibility to cross each other
 635 ($T_e = T_p$). This is indeed the case for the populations
 636 **B** and **C**. It implies that electron pressure is more effi-
 637 cient farther away from the Sun than proton pressure.
 638 However, this provides only a weak wind acceleration
 639 (Figure 4a).

4. CONCLUSION

641 In this paper we have analysed proton and electron so-
 642 lar wind measurements from the instruments SPAN-Ai,
 643 SPC and SPAN-E of PSP. We define five wind popula-
 644 tions with the same methodology than the one proposed
 645 by Maksimovic et al. (2020) for the Helios data. We use
 646 the overlap distance range of the missions to define the
 647 percentage of PSP observations representative of each
 648 Helios wind population.

649 We find a good agreement between the Helios and PSP
 650 wind profiles for the speed, electron density, proton and
 651 electron temperature. The continuous acceleration of
 652 the slow solar wind, already shown with Helios data,
 653 is also present closer to the Sun in PSP observations.
 654 Moreover the correlation bulk speed/proton tempera-
 655 ture (u , T_p) and the anti-correlation bulk speed/electron
 656 temperature (u , T_e), observed at 1 au, are maintained
 657 in the PSP observations at least as close as $20 R_\odot$ (\sim
 658 0.1 au).

659 The polytropic decrease of proton and electron tem-
 660 peratures, previously reported with Helios observations,
 661 is extended to the PSP radial range with almost the
 662 same polytropic indexes. We have modeled these regions
 663 with a fluid approach including separate polytropic be-
 664 haviours for protons and electrons. We have no clear evi-
 665 dence that this behaviour changes closer to the Sun with
 666 the most recent PSP observations. In order to avoid ex-
 667 cessively large coronal temperatures in the model, we
 668 impose the polytropic increase of both temperatures to
 669 stop at some radial distance, different for electrons and
 670 protons. At smaller distances, we simply impose con-
 671 stant temperatures.

672 The free parameters of the iso-poly model are describ-
 673 ing both proton and electron temperature radial profiles.
 674 These parameters are determined by a least square fit of
 675 the model to the data for $r < 0.5$ au. This procedure is
 676 fully successful to define a model well representing the
 677 intermediate solar winds (from 350 - 500 km/s at 1 au).
 678 Indeed, the closeness of the model to the data shows
 679 that the observed temperature gradients are sufficient
 680 to accelerate such winds with no extra energy required
 681 **in the 0.1 au - 1 au studied range. However,**
 682 **these results on iso-poly modeling of the moder-**
 683 **ate solar winds occur after the main acceleration**
 684 **region, i.e. the models are not constrained below**
 685 **0.1 au. Our study thus brings a partial answer to**
 686 **the general problem of the solar wind accelera-**
 687 **tion, which must be completed by measurements**
 688 **closer to the Sun.**

689 The observations of the slowest wind population show
 690 an acceleration over all the observed solar distances.
 691 The iso-poly model, fitted to the data for $r < 0.5$ au,
 692 is only able to account for the observed acceleration in
 693 this radial range, but not at larger distances. This result
 694 indicates the presence of another source of acceleration

695 which does not heat the plasma and operates on large
 696 solar distances, mainly for the slowest solar wind.

697 The observed fast wind profiles can be correctly re-
 698 produced by the iso-poly model for the Helios data (no
 699 PSP data are available for such winds). Nevertheless,
 700 the high needed coronal temperature (5 - 6 MK), do
 701 not allow to go deeper in the interpretation of the iso-
 702 poly modeling results. Indeed, it would require a more
 703 complete observational study of the coronal hole tem-
 704 peratures, in order to better estimate the reliability of
 705 such modeled coronal temperatures.

706 We also have found that the electron pressure is dom-
 707 inant, over the proton one, to accelerate the slow winds.
 708 This predominance increases with the solar distance.
 709 For intermediate wind speeds, the proton pressure is
 710 able to provide the main acceleration close to the Sun.
 711 In contrast, the proton pressure is dominant, while not
 712 sufficient, to accelerate the fastest wind.

713 This paper raises interesting questions about the large
 714 distance acceleration processes in the solar wind, as well
 715 as about the missing energy to the plasma heating, nec-
 716 essary to describe the observed radial evolution of the
 717 slow wind. Indeed, several physical phenomena are can-
 718 didates to explain a slight acceleration of the solar wind,
 719 such as co-rotating interaction regions, Alfvén waves,
 720 and ambipolar scattering. However, the weight of their
 721 respective role in the wind acceleration must be clarified.

722 **The data sources are :**

723 <https://doi.org/10.48322/49we-tr31> (SPC),
 724 <https://doi.org/10.48322/ypyh-s325> (SPAN-A),
 725 <https://doi.org/10.48322/8ync-7p95> (SPAN-E),
 726 <https://spdf.gsfc.nasa.gov/pub/data/helios/>
 727 (HELIOS).
 728

ACKNOWLEDGMENTS

We acknowledge the NASA Parker Solar Probe Mission and the SWEAP team led by J. Kasper for use of data, and we thank Parker Solar Probe team for valuable discussions. This work was supported by CNRS Occitanie Ouest, CNES and LESIA. We recognise the collaborative and open nature of knowledge creation and dissemination, under the control of the academic community as expressed by Camille Noûs at <http://www.cogitamus.fr/indexen.html>.

A. PARKER SOLAR PROBE TEMPERATURE ADJUSTMENT BETWEEN SPAN-AI AND SPC INSTRUMENTS

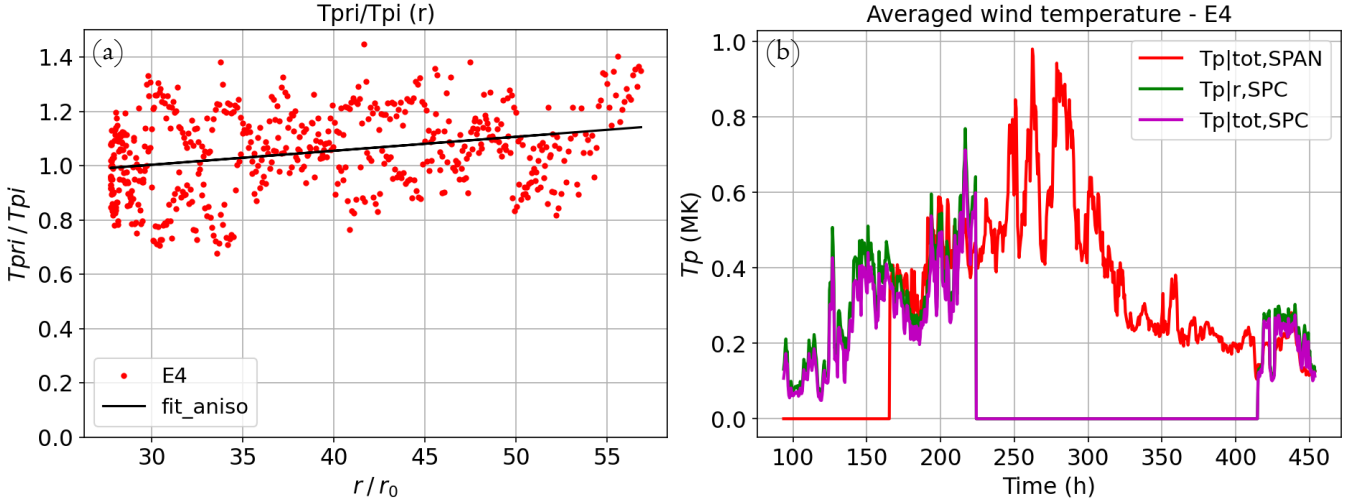


Figure 6. (a) : SPAN temperature anisotropy $T_{p|r}/T_{p|tot}$ (r) over the operating SPAN radial range (red dots), and least square linear fit (solid line). (b) : SPC radial temperature previously adjusted by a factor 2 as mentioned in Section 2.2 (green), total SPAN temperature (red), and equivalent SPC total temperature using the anisotropy relation between the radial and total temperature from SPAN (purple).

To have compatible temperatures measured by SPI and SPC covering the largest range of solar distances, we have calibrated SPC temperature with the SPI one using the ratio $T_{r|SPI}/T_{tot|SPI}$ which evolves linearly with solar distance. The panel (a) of Figure 6 show the distribution of the ratio for the measurements of the encounter 4 (red dots), and a linear adjustment of the form $y = ax + b$ applied to these measurements (solid line). The panel (b) show the SPC temperature adjustment. The equivalent total proton temperature $T_{tot|SPC}$ (purple curve) is established dividing the radial temperature $T_{r|SPC}$ (green curve) by the anisotropy linear law, assuming the law is extended over the distances covered by SPC. The equivalent total temperature from SPC data extend the SPI one (red curve) on larger distances. Finally, a unique PSP proton data set is created, associating one time to a unique parameter measurement, so for time where both SPI and SPC measurements are available, the mean value between these two is kept.

B. ISO-POLY MODEL DETAILED EQUATIONS

In this appendix, we detail the calculation of the iso-poly model. We remind that in the iso-poly description, we limit the γ_s to two regions with constant values. We start from the momentum equation (4):

$$n m_p u \frac{du}{dr} = - \sum_{s=\{p,e\}} \left(P_{s,iso|s} \frac{d\tilde{n}_s^{\gamma_s}}{dr} \right) - n m_p \frac{GM}{r^2}, \quad (\text{B1})$$

where $\tilde{n}_s = n(r)/n_{iso|s}$.

We use the properties of the logarithmic derivative of a composite function to compute:

$$\frac{d\tilde{n}_s^{\gamma_s}}{dr} = \tilde{n}_s^{\gamma_s} \frac{d(\gamma_s \ln(\tilde{n}_s))}{dr} = \gamma_s \tilde{n}_s^{\gamma_s-1} \frac{d\tilde{n}_s}{dr} + \tilde{n}_s^{\gamma_s} \ln(\tilde{n}_s) \frac{d\gamma_s}{dr} \quad (\text{B2})$$

Since we set γ_s constant in the isotherm and polytropic regions $d\gamma_s/dr = 0$. The momentum Equation (B1) is rewritten as:

$$n u \frac{du}{dr} = - \sum_{s=\{p,e\}} \left(\frac{P_{s,iso|s}}{m_p} \gamma_s \tilde{n}_s^{\gamma_s-1} \frac{d\tilde{n}_s}{dr} \right) - n \frac{GM}{r^2} \quad (\text{B3})$$

To further simplify the equation writing, we define c_s for the species s as an equivalent sound speed:

$$c_s^2 = \frac{\gamma_s P_{s,\text{iso}|s}}{m_p n_{\text{iso}|s}} = \frac{\gamma_s k_B T_{s,\text{iso}|s}}{m_p} \quad (\text{B4})$$

We also define the variable x_s with $x_s = \tilde{n}_s^{\gamma_s - 1}$. With the above definitions, we obtain:

$$n u \frac{du}{dr} = - \sum_{s=\{\text{p,e}\}} n_{\text{iso}|s} \left(c_s^2 x_s \frac{d\tilde{n}_s}{dr} \right) - n \frac{GM}{r^2} \quad (\text{B5})$$

Next, the conservation of mass flux writes as $n(r) = C_n / (ur^2)$, where C_n a constant. Developing the calculation of the derivative of $\tilde{n}_s(r)$:

$$\frac{d\tilde{n}_s}{dr} = - \frac{1}{n_{\text{iso}|s}} \frac{C_n}{r^2} \left[\frac{2}{ur} + \frac{1}{u^2} \frac{du}{dr} \right] \quad (\text{B6})$$

Finally, the momentum equation is written as:

$$\frac{du}{dr} \left[\frac{C_n}{ur^2} u - \sum_{s=\{\text{p,e}\}} \frac{C_n}{r^2} \frac{c_s^2}{u^2} x_s \right] = \sum_{s=\{\text{p,e}\}} \left[\frac{C_n}{r^2} \frac{2}{ur} c_s^2 x_s \right] - \frac{C_n}{ur^2} \frac{GM}{r^2} \quad (\text{B7})$$

$$\Rightarrow \underbrace{\frac{du}{dr} \left[1 - \sum_{s=\{\text{p,e}\}} \frac{c_s^2}{u^2} x_s \right]}_{a(r,u)} = \frac{1}{ur} \underbrace{\left[\sum_{s=\{\text{p,e}\}} 2c_s^2 x_s - \frac{GM}{r} \right]}_{b(r,u)} \quad (\text{B8})$$

743 The equation (B8) summarizes the iso-poly model. The solar wind flow is described by the transonic solution with
 744 $du/dr \neq 0$ for all r values. Then, where $b(r, u) = 0$, $a(r, u)$ should also vanishes. This defines the so called critical or
 745 sonic point. If it is located in the isothermal region $x_s = 1$, and the critical point is defined by the isothermal Parker's
 746 result:

$$u_c = \sqrt{c_p^2 + c_e^2} \quad \text{and} \quad r_c = \frac{GM}{2(c_p^2 + c_e^2)} \quad (\text{B9})$$

747 with c_p and c_e computed with Equation (B4) and $\gamma_s = 1$. In the polytropic region, the critical radius r_c is divided
 748 by the factor $\gamma_s > 1$ compared to Equation (B9). When we fit the iso-poly model to observations (Section 3.3), the
 749 optimum r_c value stays within the isothermal region. Moreover, if during the fitting iteration r_c goes a bit in the
 750 polytropic region, its value is divided by γ_s , which bring it back to the isothermal region. The temperatures $T_p(r_c)$
 751 and $T_e(r_c)$ would need to be significantly lower than T_{s0} to keep r_c in the polytropic region.

752 The optimal way to compute the transonic solution is to use an asymptotic development around r_c of the equation
 753 (B8) to get the slope du/dr at the critical point. In fact, we proceed simpler using a tiny positive (resp. negative)
 754 shift from (r_c, u_c) to integrate upward (resp. downward). With a tiny shift such solutions converge rapidly toward the
 755 transonic solution, thanks to the hyperbolic topology present around the critical point. Finally, with $u(r)$ computed,
 756 the density expression is deduced from mass flux conservation, and the temperature radial profile of the species is
 757 defined by Equation (1).

C. DETERMINATION OF ISO-POLY PARAMETERS WITH THE CHI-SQUARED TEST

758 We outline below the determination of the free parameters for the iso-poly model. First the modeled temperature
 759 profile are least square fitted to each observed profile. This defines the polytropic indexes γ_p and γ_e . To be in
 760 accordance with the in-situ measured temperature, we constrain for each population of the model, the minimal coronal
 761 temperature T_{s0} to the closest radially observed temperature. Next, the model bulk speed is compared to observed
 762 velocities for different $(r_{\text{iso}|p}, r_{\text{iso}|e})$ values, and for each wind population. The resulting χ^2 minimization map $(r_{\text{iso}|p},$
 763 $r_{\text{iso}|e})$ for the population **A** and **E** are plotted on Figure 7. With the supposed continuity of the temperature profiles,
 764 this also determines the coronal temperatures T_{p0} and T_{e0} (supposed to be uniform below $r_{\text{iso}|p}$ and $r_{\text{iso}|e}$, respectively).
 765

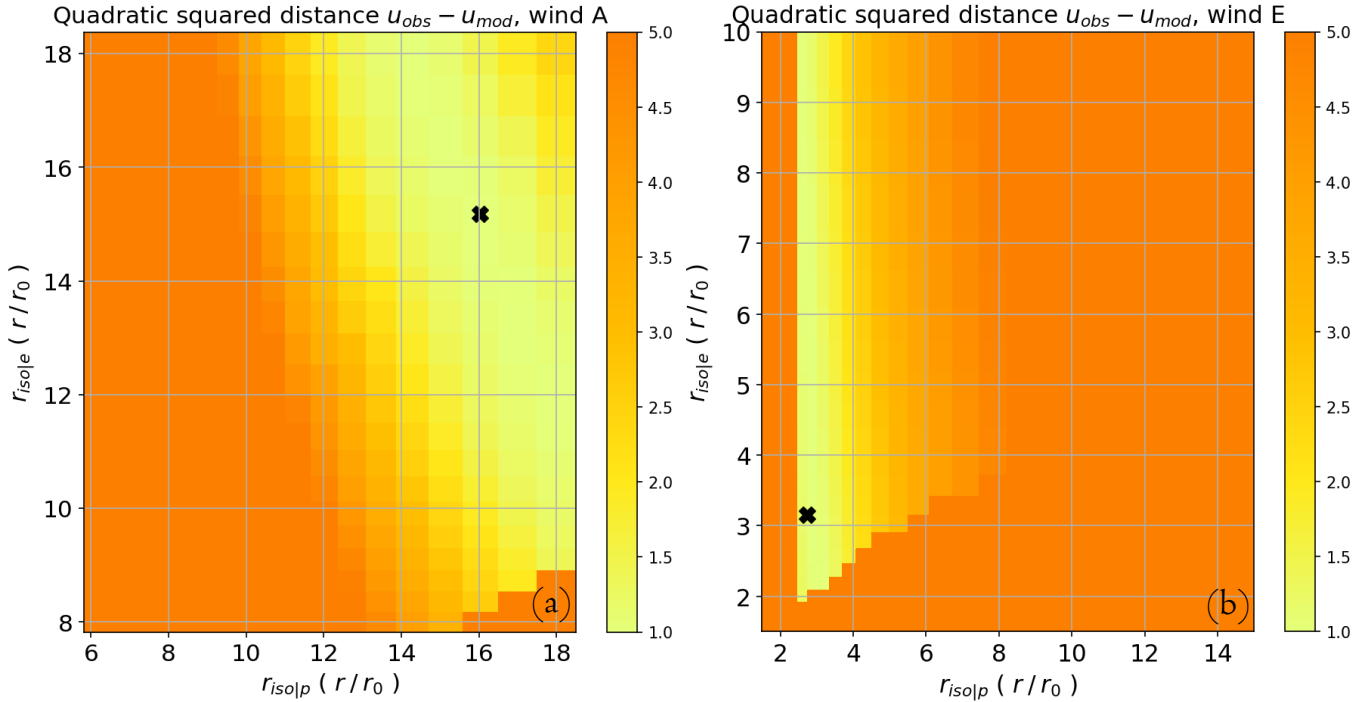


Figure 7. χ^2 values expressing the distance between the iso-poly model and the solar wind data within the $(r_{\text{isolep}}, r_{\text{isole}})$ plane. (a) the slowest population A (Helios-PSP data), (b) the fastest population E (Helios data). The black crosses represents the location of the best set of parameters (main minimum of $\chi^2(r_{\text{isolep}}, r_{\text{isole}})$).

766 The optimal set of parameters is not located in a spot minimum region of the map, but in a valley. For the wind **A**
 767 both r_{isole} and r_{isolep} values have an influence, because the valley is diagonally oriented. The smaller r_{isolep} is, the bigger
 768 r_{isole} is, so that they compensate each other to fit as best as possible to the observed speed profile. Indeed, Figure 5
 769 shows that $T_p \approx T_e$, so $P_p \approx P_e$ in the main acceleration region ($r < 20R_\odot$). In contrast, the wind **E** minimization
 770 maps shows a region of smaller values on a more vertically oriented valley, signifying that the value of r_{isolep} is well
 771 determined, and thus is more determinant in the modeling of fast wind than r_{isole} . Indeed, Figure 5 shows that T_p ,
 772 then P_p , is dominant for wind **E** in the main acceleration region.

REFERENCES

- 773 Cranmer, S. R. 2002, *SSRv*, 101, 229,
 774 doi: [10.1023/A:1020840004535](https://doi.org/10.1023/A:1020840004535)
- 775 Cranmer, S. R., Field, G. B., & Kohl, J. L. 1999, *ApJ*, 518,
 776 937, doi: [10.1086/307330](https://doi.org/10.1086/307330)
- 777 Cranmer, S. R., Matthaeus, W. H., Breech, B. A., &
 778 Kasper, J. C. 2009, *ApJ*, 702, 1604,
 779 doi: [10.1088/0004-637X/702/2/1604](https://doi.org/10.1088/0004-637X/702/2/1604)
- 780 David, C., Gabriel, A. H., Bely-Dubau, F., et al. 1998,
 781 *A&A*, 336, L90
- 782 Démoulin, P. 2009, *SoPh*, 257, 169,
 783 doi: [10.1007/s11207-009-9338-5](https://doi.org/10.1007/s11207-009-9338-5)
- 784 Elliott, H. A., Henney, C. J., McComas, D. J., Smith,
 785 C. W., & Vasquez, B. J. 2012, *Journal of Geophysical*
 786 *Research (Space Physics)*, 117, A09102,
 787 doi: [10.1029/2011JA017125](https://doi.org/10.1029/2011JA017125)
- 788 Esser, R., Habbal, S. R., Coles, W. A., & Hollweg, J. V.
 789 1997, *J. Geophys. Res.*, 102, 7063,
 790 doi: [10.1029/97JA00065](https://doi.org/10.1029/97JA00065)
- 791 Fox, N. J., Velli, M. C., Bale, S. D., et al. 2016, *SSRv*, 204,
 792 7, doi: [10.1007/s11214-015-0211-6](https://doi.org/10.1007/s11214-015-0211-6)
- 793 Gloeckler, G., Zurbuchen, T. H., & Geiss, J. 2003, *Journal*
 794 *of Geophysical Research (Space Physics)*, 108, 1158,
 795 doi: [10.1029/2002JA009286](https://doi.org/10.1029/2002JA009286)
- 796 Halekas, J. S. 2022, in press, *ApJS*
- 797 Halekas, J. S., Whittlesey, P., Larson, D. E., et al. 2020,
 798 *ApJS*, 246, 22, doi: [10.3847/1538-4365/ab4cec](https://doi.org/10.3847/1538-4365/ab4cec)
- 799 Hellinger, P., Matteini, L., Štverák, Š., Trávníček, P. M., &
 800 Marsch, E. 2011, *Journal of Geophysical Research (Space*
 801 *Physics)*, 116, A09105, doi: [10.1029/2011JA016674](https://doi.org/10.1029/2011JA016674)

- 802 Hellinger, P., Trávníček, P. M., Štverák, Š., Matteini, L., &
803 Velli, M. 2013, *Journal of Geophysical Research (Space*
804 *Physics)*, 118, 1351, doi: [10.1002/jgra.50107](https://doi.org/10.1002/jgra.50107)
805 Kasper, J. C., Abiad, R., Austin, G., et al. 2016, *SSRv*,
806 204, 131, doi: [10.1007/s11214-015-0206-3](https://doi.org/10.1007/s11214-015-0206-3)
807 Kohl, J. L., Strachan, L., & Gardner, L. D. 1996, *ApJL*,
808 465, L141, doi: [10.1086/310145](https://doi.org/10.1086/310145)
809 Lopez, R. E., & Freeman, J. W. 1986, *J. Geophys. Res.*, 91,
810 1701, doi: [10.1029/JA091iA02p01701](https://doi.org/10.1029/JA091iA02p01701)
811 Maksimovic, M., Bale, S. D., Berčić, L., et al. 2020, *ApJS*,
812 246, 62, doi: [10.3847/1538-4365/ab61fc](https://doi.org/10.3847/1538-4365/ab61fc)
813 Marsch, E., Pilipp, W. G., Thieme, K. M., & Rosenbauer,
814 H. 1989, *J. Geophys. Res.*, 94, 6893,
815 doi: [10.1029/JA094iA06p06893](https://doi.org/10.1029/JA094iA06p06893)
816 Parker, E. N. 1958, *ApJ*, 128, 664, doi: [10.1086/146579](https://doi.org/10.1086/146579)
817 —. 1960, *ApJ*, 132, 821, doi: [10.1086/146985](https://doi.org/10.1086/146985)
818 Porsche, H. 1981, in *ESA Special Publication, Vol. 164,*
819 *Solar System and its Exploration*, ed. W. R. Burke, 43–50
820 Quémerais, E., & Lamy, P. 2002, *A&A*, 393, 295,
821 doi: [10.1051/0004-6361:20021019](https://doi.org/10.1051/0004-6361:20021019)
822 Sanchez-Diaz, E., Rouillard, A. P., Lavraud, B., et al. 2016,
823 *Journal of Geophysical Research (Space Physics)*, 121,
824 2830, doi: [10.1002/2016JA022433](https://doi.org/10.1002/2016JA022433)
825 Schwartz, S. J., & Marsch, E. 1983, *J. Geophys. Res.*, 88,
826 9919, doi: [10.1029/JA088iA12p09919](https://doi.org/10.1029/JA088iA12p09919)
827 Schwenn, R., Rosenbauer, H., & Miggenrieder, H. 1975,
828 *Raumfahrtforschung*, 19, 226
829 Sheeley, N. R., Wang, Y. M., Hawley, S. H., et al. 1997,
830 *ApJ*, 484, 472, doi: [10.1086/304338](https://doi.org/10.1086/304338)
831 Totten, T. L., Freeman, J. W., & Arya, S. 1995,
832 *J. Geophys. Res.*, 100, 13, doi: [10.1029/94JA02420](https://doi.org/10.1029/94JA02420)
833 Štverák, Š. t., Trávníček, P. M., & Hellinger, P. 2015,
834 *Journal of Geophysical Research (Space Physics)*, 120,
835 8177, doi: [10.1002/2015JA021368](https://doi.org/10.1002/2015JA021368)
836 Štverák, Š., Maksimovic, M., Trávníček, P. M., et al. 2009,
837 *Journal of Geophysical Research (Space Physics)*, 114,
838 A05104, doi: [10.1029/2008JA013883](https://doi.org/10.1029/2008JA013883)